

Guidelines for accurate and efficient calculations of mobilities in two-dimensional materials

Jiaqi Zhou,^{1,*} Samuel Poncé,^{1,2,3,†} and Jean-Christophe Charlier^{1,‡}

¹*Institute of Condensed Matter and Nanosciences (IMCN),
Université catholique de Louvain (UCLouvain), 1348 Louvain-la-Neuve, Belgium*

²*European Theoretical Spectroscopy Facility*

³*WEL Research Institute, Avenue Pasteur 6, 1300 Wavre, Belgium*

(Dated: April 16, 2024)

Emerging two-dimensional (2D) materials bring unprecedented opportunities for electronic applications. The design of high-performance devices requires an accurate prediction of carrier mobility in 2D materials, which can be obtained using state-of-the-art *ab initio* calculations. However, various factors impact the computational accuracy, leading to contradictory estimations for the mobility. In this work, targeting accurate and efficient *ab initio* calculations, transport properties in III-V monolayers are reported using the Boltzmann transport equation, and the influences of pseudopotential, quadrupole correction, Berry connection, and spin-orbit coupling (SOC) on mobilities are systematically investigated. Our findings are as follows: (1) The inclusion of semi-core states in pseudopotentials is important to obtain accurate calculations. (2) The variations induced by dynamical quadrupole and Berry connection when treating long range fields can be respectively 40% and 10%. (3) The impact of SOC can reach up to 100% for materials with multi-peak bands. Importantly, although SOC notably modifies the electronic wavefunctions, it negligibly impacts the dynamical matrices and scattering potential variations. As a result, the combination of fully-relativistic electron calculation and scalar-relativistic phonon calculation can strike a good balance between accuracy and cost. This work compares computational methodologies, providing guidelines for accurate and efficient calculations of mobilities in 2D semiconductors.

I. INTRODUCTION

Two-dimensional (2D) materials exhibit exotic phenomena which can be used in electronic and spintronic devices [1–3]. The atomical thickness of 2D semiconductors enables the efficient engineering of electronic properties through gate voltage control, making them promising for transistor applications [4, 5]. Drift mobility quantifies the transport of carrier in a material in response to an electric field, and the prediction of carrier mobility is critical for the design of high-performance devices. A prevalent approach is to employ density functional theory (DFT) and density functional perturbation theory (DFPT) to evaluate the electron-phonon coupling (EPC) matrices [6]. However, the accurate calculation of mobility requires very dense momentum grids, which is generally too expensive to be performed by direct DFPT calculations. To solve the problem of computational cost, Wannier functions can be used to interpolate EPC from coarse grids to fine grids [7]. Using this technique, efforts have been devoted to discovering 2D materials with high mobilities [8–13]. However, conclusions are found to be contradictory due to the various approximations used in different studies. A high-throughput work reports that III-V monolayers with atomically flat structures can present high electron mobility (μ^e) and high hole mobility (μ^h). For example, in the case of Bsb monolayer, Refs. [14] and [15] report a higher hole mobility (μ^h) than electron mobility (μ^e) with different values: $\mu^h/\mu^e = 6935/5167 \text{ cm}^2/\text{Vs}$ [14] and $\mu^h/\mu^e = 16397/9520 \text{ cm}^2/\text{Vs}$ [15]. In contrast, Ref. [16] finds a larger $\mu^e = 16221$ than $\mu^h = 7882 \text{ cm}^2/\text{Vs}$. These discrepancies illustrate that an accurate prediction for carrier mobility can be complicated since many factors are involved, creating

confusion on *ab initio* values of computed mobilities in 2D materials.

The atomic motions in 2D semiconductors generate long-range dynamical dipole and quadrupole that should be considered to accurately interpolate EPC. Moreover, spin-orbit coupling (SOC) can significantly modify the electronic structures in materials with heavy elements. The semi-core states in pseudopotentials may also influence the hole effective mass. To understand and facilitate the computation, it is necessary to elucidate the impacts on the mobilities in 2D materials caused by these factors in order to optimize the balance between the accuracy and the computational cost in *ab initio* calculations.

In this work, we focus on the III-V monolayers MX (M = Ga, In and X = P, As, Sb) considering the moderate bandgap and SOC strength. The influences on mobilities caused by pseudopotentials with different semi-core states [17], dynamical quadrupole [18–20], Berry connection [12, 21], and SOC are systematically studied. Their impacts are interpreted by investigating the momentum- and mode-resolved scattering rates. Besides, DFPT results are found to be negligibly affected by SOC, thus it can be neglected to accelerate computation. After discussing methodologies, the temperature-dependent drift and Hall mobilities are computed. Rather than the unity which is commonly assumed in experiments, it is found that the Hall factors range from 1.0 to 1.7.

II. DRIFT MOBILITY

The phonon-limited drift mobility of carrier in 2D semiconductor is calculated as [22, 23]:

$$\mu_{\alpha\beta} = \frac{-1}{S_{uc}n_c} \sum_n \int \frac{d^2\mathbf{k}}{\Omega_{BZ}} v_{n\mathbf{k}\alpha} \partial_{E_\beta} f_{nk}, \quad (1)$$

* jiaqi.zhou@uclouvain.be

† samuel.ponce@uclouvain.be

‡ jean-christophe.charlier@uclouvain.be

TABLE I. Methodologies employed in this work. PP is the abbreviation for pseudopotential. Quad and Berry respectively indicate whether dynamical quadrupole and Berry connection are considered. FR denotes the fully-relativistic calculation with SOC, while SR denotes the scalar-relativistic calculation without SOC. e denotes the treatment of electronic calculation for wavefunctions, and ph denotes the treatment of phonon calculation for scattering potential variations. The methodology #7 strikes a good balance between accuracy and cost when a “mix” approach is used for the treatment of e and ph .

Number	Methodology notation	PP	Quad	Berry	e	ph
#1	valencePP+Quad+Berry+FR	valence	Yes	Yes	FR	FR
#2	standardPP+Quad+Berry+FR	standard	Yes	Yes	FR	FR
#3	stringentPP+Quad+Berry+FR	stringent	Yes	Yes	FR	FR
#4	standardPP+Quad+FR	standard	Yes	No	FR	FR
#5	standardPP+FR	standard	No	No	FR	FR
#6	standardPP+Quad+Berry+SR	standard	Yes	Yes	SR	SR
#7	standardPP+Quad+Berry+mix	standard	Yes	Yes	FR	SR

where α, β are Cartesian directions and $\alpha = \beta$ in the plane for the III-V monolayers. The $\partial_{E_\beta} f_{nk} = (\partial f_{nk} / \partial E_\beta) |_{\mathbf{E}=0}$ indicates the linear variation of the electronic occupation function f_{nk} in response to the electric field \mathbf{E} . S^{uc} is the unit cell area, and Ω^{BZ} the first Brillouin zone (BZ) area. The band velocity of state ε_{nk} is given by $v_{nk\alpha} = \hbar^{-1} \partial \varepsilon_{nk} / \partial k_\alpha$, and n^c denotes the carrier concentration in a vanishing limit. $\partial_{E_\beta} f_{nk}$ can be obtained by solving the linearized Boltzmann transport equation (BTE) [23]:

$$\begin{aligned} \partial_{E_\beta} f_{nk} = & e v_{nk\beta} \frac{\partial f_{nk}^0}{\partial \varepsilon_{nk}} \tau_{nk} + \frac{2\pi\tau_{nk}}{\hbar} \sum_{m\nu} \int \frac{d^2\mathbf{q}}{\Omega^{\text{BZ}}} |g_{m\nu}(\mathbf{k}, \mathbf{q})|^2 \\ & \times \left[(n_{\mathbf{q}\nu} + 1 - f_{nk}^0) \delta(\varepsilon_{nk} - \varepsilon_{m\mathbf{k}+\mathbf{q}} + \hbar\omega_{\mathbf{q}\nu}) \right. \\ & \left. + (n_{\mathbf{q}\nu} + f_{nk}^0) \delta(\varepsilon_{nk} - \varepsilon_{m\mathbf{k}+\mathbf{q}} - \hbar\omega_{\mathbf{q}\nu}) \right] \partial_{E_\beta} f_{m\mathbf{k}+\mathbf{q}}, \end{aligned}$$

where τ_{nk} is the total scattering lifetime, and its inverse τ_{nk}^{-1} is the scattering rate, given as

$$\begin{aligned} \tau_{nk}^{-1} = & \frac{2\pi}{\hbar} \sum_{m\nu} \int \frac{d^2\mathbf{q}}{\Omega^{\text{BZ}}} |g_{m\nu}(\mathbf{k}, \mathbf{q})|^2 \\ & \times \left[(n_{\mathbf{q}\nu} + 1 - f_{m\mathbf{k}+\mathbf{q}}^0) \delta(\varepsilon_{nk} - \varepsilon_{m\mathbf{k}+\mathbf{q}} - \hbar\omega_{\mathbf{q}\nu}) \right. \\ & \left. + (n_{\mathbf{q}\nu} + f_{m\mathbf{k}+\mathbf{q}}^0) \delta(\varepsilon_{nk} - \varepsilon_{m\mathbf{k}+\mathbf{q}} + \hbar\omega_{\mathbf{q}\nu}) \right], \end{aligned} \quad (2)$$

where $g_{m\nu}(\mathbf{k}, \mathbf{q})$ is the EPC matrix element denoting the amplitude of scattering between the $|nk\rangle$ state and the $|m\mathbf{k}+\mathbf{q}\rangle$ state via the phonon of frequency $\omega_{\mathbf{q}\nu}$, $n_{\mathbf{q}\nu}$ is the Bose-Einstein distribution, and f_{nk}^0 is the Fermi-Dirac occupation function.

III. COMPUTATIONAL DETAILS

To solve these equations, we compute wavefunctions and potential variations using the QUANTUM ESPRESSO package [24]. The norm-conserving pseudopotentials PSEUDO DOJO [17] have been employed within the Perdew-Burke-Ernzerhof (PBE) parametrization of the generalized gradient approximation (GGA) [17]. Variable cell relaxation is performed with total energy convergence of 10^{-8} Ry, force conver-

gence of 10^{-4} Ry/Bohr, and pressure convergence of 0.1 kbar. The cutoff energy for wavefunctions is set to 120 Ry. We use the 2D Coulomb truncation scheme of Ref. [25] with a vacuum distance over 19 Å. Note that in the calculation at the zone-center $\mathbf{q} = \Gamma$, a denser \mathbf{k} -grid is used in DFPT to get convergent electrostatic properties. Electron and hole mobilities are calculated using the EPW package [26, 27], where the electron-phonon coupling is interpolated from coarse \mathbf{k}/\mathbf{q} -grids to fine \mathbf{k}/\mathbf{q} -grids using Wannier functions with the considerations of dipole, quadrupole, and Berry connection [12, 21]. A coarse $12 \times 12 \times 1$ \mathbf{k}/\mathbf{q} -grid is adopted in *ab initio* calculations, then a fine \mathbf{k}/\mathbf{q} -grid of $720 \times 720 \times 1$ is used for electron mobility, and \mathbf{k}/\mathbf{q} -grid of $360 \times 360 \times 1$ for hole mobility. A Fermi surface window of 0.3 eV is used in all calculations. Convergence tests have been performed with respect to the grid density and Fermi surface window. An adaptive smearing is applied in the energy-conserving delta functions, and a phonon frequency cutoff of 1 cm^{-1} is employed. The temperature is set at 300 K if not mentioned. The dynamical quadrupole is computed using linear response as implemented in ABINIT [28, 29] with a \mathbf{k} -grid of $32 \times 32 \times 1$, together with the PSEUDO DOJO pseudopotentials without non-linear core corrections or spin-orbit coupling [30]. For reproducibility, all information including input files, software, pseudopotentials, and additional details are provided on the Materials Cloud Archive [31].

IV. METHODOLOGY

In the present section, we focus on the impacts on mobilities induced by pseudopotentials, dynamical quadrupole, Berry connection, and SOC. Using the stringent pseudopotential table from PSEUDO DOJO [17] and considering SOC, the atomic structures of all the materials have been relaxed. We find that all the III-V monolayers present a buckled structure, in agreement with Refs. [16, 32–34]. This buckling breaks the inversion symmetry, leading to a Rashba splitting when SOC is considered. Details related to atomic structures are given in Section S1 in the Supplemental Material (SM) [35]. InAs monolayer is taken as a representative material due to its moderate bandgap and SOC strength. Results for the other monolayers can be found in SM [35]. Methodologies are listed in Table I. Three types

of control experiments are implemented for the drift mobility calculations, respectively evaluating the impacts of pseudopotentials (#1, #2, and #3), dynamical quadrupole and Berry connection (#2, #4, and #5), and fully-relativistic SOC effect (#2 and #6). Another evaluation is performed for the computational efficiency (#2 and #7) by employing the wavefunctions from the fully-relativistic calculation and the scattering potential variation from the scalar-relativistic calculation.

IV.1. Impact of pseudopotential

Three types of norm-conserving pseudopotentials from PSEUDO DOJO are used in this work. For elements with the principal quantum number $n \geq 3$, the valence pseudopotential only includes the valence electrons, the standard pseudopotential includes one full d orbital, and the stringent pseudopotential includes full s , p , and d orbitals. Details of included orbitals can be found in Table S2 in SM [35].

Figure 1 shows the electron and phonon dispersions of InAs monolayer computed by valence, standard, and stringent pseudopotentials, respectively. Different pseudopotentials introduce small changes to the valence bands. The valence band maximum (VBM) is always located at the Γ point. For the valence pseudopotential, $\varepsilon_K = E_F - 140$ meV. However, for the standard and stringent pseudopotentials, the highest valence band presents $\varepsilon_K \approx E_F - 90$ meV, demonstrating that the semi-core

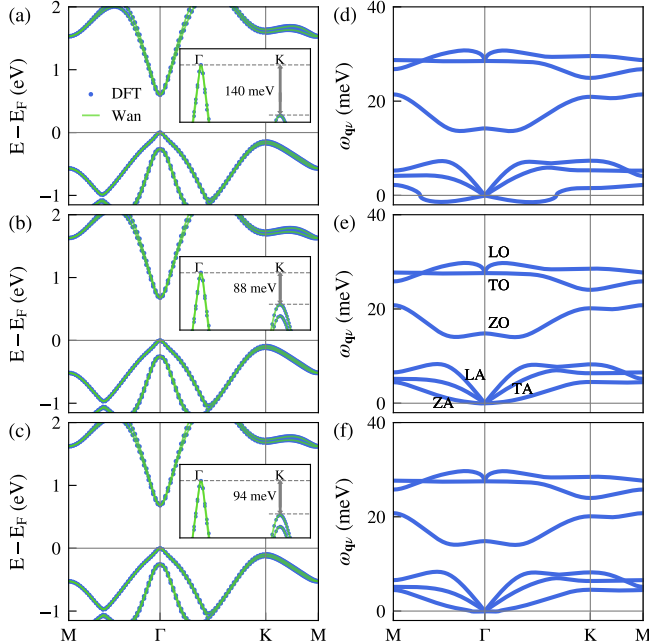


FIG. 1. InAs monolayer electronic band structures (a)-(c) and phonon dispersions (d)-(f) for fully-relativistic calculations of valence, standard, and stringent pseudopotentials, respectively. The insets in (a)-(c) show a zoomed-in figure around the Fermi energy. Phonon modes are marked by ZA for the out-of-plane acoustic mode, TA for the transverse acoustic mode, LA for the longitudinal acoustic mode, ZO for the out-of-plane optical mode, TO for the transverse optical mode, and LO for the longitudinal optical mode.

states can cause a discrepancy of 50 meV on the valence bands. More intriguingly, phonon dispersions are strongly affected as illustrated in Figs. 1(d)-(f). Imaginary frequencies emerge around the Γ point in the valence pseudopotential calculation. Besides, the translational invariance is violated by the stringent pseudopotential, and the former can be recovered by the acoustic sum rule as demonstrated by Fig. S9 in SM [35]. Overall, the quadratic ZA mode is derived with the standard pseudopotential.

The convergence of mobility requires a fine grid to sample BZ, making DFPT calculation too expensive to be afforded. Thus, maximally localized Wannier functions (MLWFs) are used for EPC calculation. To assess the quality of the Wannier interpolation, we compare the interpolated band structures in Figs. 1(a)-(c), and EPC matrix element with those obtained from a direct DFPT calculation. For simplicity, we compute the total deformation potential [36] in the BZ center zone:

$$D_\nu(\Gamma, \mathbf{q}) = \frac{1}{\hbar N^w} \left[2\rho\Omega\hbar\omega_{\mathbf{q}\nu} \sum_{nm} |g_{mn\nu}(\Gamma, \mathbf{q})|^2 \right]^{1/2}, \quad (3)$$

where the $\mathbf{k} = \Gamma$ point is chosen, the sum over bands is carried over the N^w states of the Wannier manifold, and ρ is the mass density of the crystal. It is found that deformation potentials calculated by different pseudopotentials are quite similar, thus only the result of standard pseudopotential is presented in Fig. 2, results of valence and stringent pseudopotentials are given in Fig. S2 in SM [35]. The Wannier interpolation reproduces the direct DFPT calculation quite well, hence validating its quality as well as the following computed transport properties. It should be noted that the convergence of DFPT calculations of \mathbf{q} -points around Γ requires a denser \mathbf{k} -grid of DFT calculations. Here a $32 \times 32 \times 1$ \mathbf{k} -grid is employed at $\mathbf{q} = \Gamma$, a $18 \times 18 \times 1$ \mathbf{k} -grid is used for \mathbf{q} -points around Γ , and a $12 \times 12 \times 1$ \mathbf{k} -grid

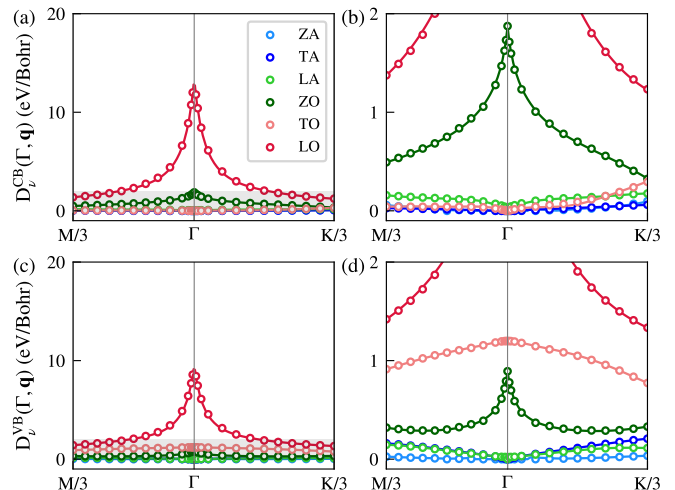


FIG. 2. Comparison between the deformation potentials of InAs monolayer with the initial state $\mathbf{k} = \Gamma$ along high-symmetry lines, the DFPT and Wannier interpolation results are respectively denoted by dots and lines. The standard pseudopotential is employed. Conduction (a) and valence (c) bands are given in the left column, the corresponding zoomed-in figures (b) and (d) of the shadowed region from 0 to 2 eV/Bohr are given in the right column.

TABLE II. Dynamical dipole Z (e) and quadrupole Q ($e\text{Bohr}$), separation length L (Bohr), dielectric and polarizability tensors (ϵ and α) of all the pristine monolayers. Only independent components are presented. Note that the crystal symmetry constants $Z_{\kappa xx} = Z_{\kappa yy}$, $Q_{\kappa xxz} = Q_{\kappa yyz}$, $Q_{\kappa xxy} = Q_{\kappa yxx} = -Q_{\kappa yyy}$, $Q_{\kappa zxx} = Q_{\kappa zyy}$, $\epsilon_{xx}^{\parallel} = \epsilon_{yy}^{\parallel}$, and $\alpha_{xx}^{\parallel} = \alpha_{yy}^{\parallel}$.

2DM	Ga	P	In	P	Ga	As	In	As	Ga	Sb	In	Sb
$Z_{\kappa xx}$	2.956	-2.956	3.223	-3.223	2.946	-2.946	3.222	-3.222	2.765	-2.765	3.039	-3.039
$Z_{\kappa zz}$	0.132	-0.132	0.153	-0.153	0.089	-0.089	0.118	-0.118	0.046	-0.046	0.075	-0.075
$Q_{\kappa xxz}$	-0.858	-1.209	-1.007	-1.809	-1.444	-1.650	-0.260	-5.396	-1.996	-1.578	-2.139	-2.110
$Q_{\kappa xxy}$	14.158	-4.579	15.039	-4.345	16.900	-7.106	18.077	-6.348	21.026	-10.996	21.485	-10.062
$Q_{\kappa zxx}$	-11.905	7.813	-17.423	11.754	-26.850	20.669	-34.642	26.327	-41.400	34.332	-45.725	37.248
$Q_{\kappa zzz}$	0.638	-0.569	0.775	-0.666	1.150	-1.070	2.599	-6.637	1.454	-1.352	1.553	-1.434
L	9.852		12.257		16.218		18.973		27.624		26.270	
$\epsilon_{xx}^{\parallel}$	3.034		3.408		3.874		4.449		5.372		5.768	
ϵ^{\perp}	1.152		1.160		1.161		1.169		1.174		1.180	
α_{xx}^{\parallel}	6.117		7.245		8.644		10.375		13.150		14.341	
α^{\perp}	0.458		0.483		0.486		0.509		0.525		0.544	

is employed for \mathbf{q} -points around M/3 and K/3.

Figure 3 displays the mobilities of the III-V monolayers. Large electron mobilities around $1000 \text{ cm}^2/\text{Vs}$ are presented, while the hole mobilities of GaP, InP, and GaAs are significantly suppressed, and relatively large μ^h are found in InAs, GaSb, and InSb. To have a more intuitive comparison, the ratios of the valence and stringent pseudopotential results to the standard pseudopotential result are displayed in Figs. 3(c) and (d), respectively for electron and hole mobilities. For the electron mobility, the variation is limited to $\sim 10\%$. For the hole mobility, considerable variations are observed: InAs monolayer presents $\eta^h = 151\%$, and two phosphides even present η^h over 200%. It should be noted that in the valence pseudopotential results, imaginary frequencies appear in the phonon dispersions of InAs, GaP, and InP monolayers as shown in Fig. 1(d), Fig. S3,

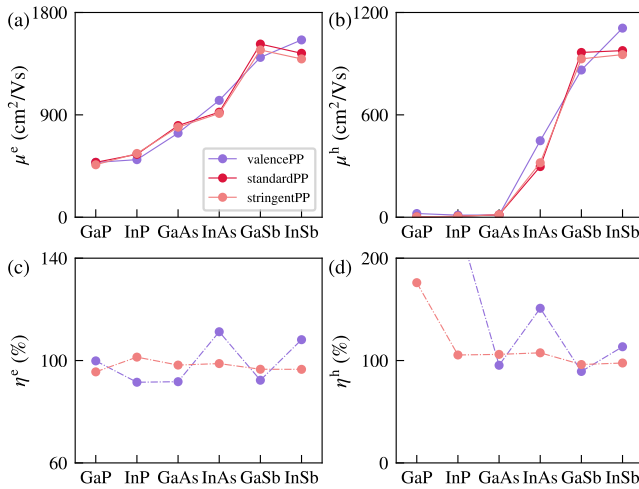


FIG. 3. Electron (a) and hole (b) mobilities calculated using different pseudopotentials according to #1, #2, and #3 methodologies. Taking the result of standard pseudopotential as a benchmark, variations of the results of valence and stringent pseudopotentials are given as ratios in (c) for electron and (d) for hole, respectively.

and Fig. S5 in SM [35], thus the calculated mobility may be questioned. Besides, the standard and stringent pseudopotentials present consistent behaviors in most cases, except for the μ^h of GaP since it is minimal thus vulnerable to numerical errors for a ratio. The above discussion shows that the semi-core states will influence the electronic structure and phonon dispersions, leading to variations in mobilities. Considering that standard and stringent pseudopotentials present consistent behaviors, applying the former can produce correct phonon dispersion without acoustic sum rule, we conclude that the standard pseudopotential is the most appropriate for mobility calculation.

IV.2. Impacts of dynamical quadrupole and Berry connection

In the case of infrared active 2D materials, the Fröhlich interaction leads to a direction-dependent $g_{m\nu}(\mathbf{k}, \mathbf{q})$ for $|\mathbf{q}| \rightarrow 0$ [37], hindering the application of Wannier interpolation. This non-analytic behavior can be solved by separating $g_{m\nu}(\mathbf{k}, \mathbf{q})$ into a short-range (\mathcal{S}) and long-range (\mathcal{L}) contribution [38], as

$$g_{m\nu}(\mathbf{k}, \mathbf{q}) = g_{m\nu}^{\mathcal{S}}(\mathbf{k}, \mathbf{q}) + g_{m\nu}^{\mathcal{L}}(\mathbf{k}, \mathbf{q}), \quad (4)$$

where the short-range part is smooth and analytic in \mathbf{q} . The non-analyticity is included in the long-range part, which is given by an explicit expression. Once it is obtained, $g_{m\nu}(\mathbf{k}, \mathbf{q})$ can be accurately calculated: firstly subtracting $g_{m\nu}^{\mathcal{L}}(\mathbf{k}, \mathbf{q})$ to obtain $g_{m\nu}^{\mathcal{S}}(\mathbf{k}, \mathbf{q})$ on the coarse grid, then applying the Wannier interpolation to $g_{m\nu}^{\mathcal{S}}(\mathbf{k}, \mathbf{q})$, and finally adding back $g_{m\nu}^{\mathcal{L}}(\mathbf{k}, \mathbf{q})$ to the interpolated $g_{m\nu}^{\mathcal{S}}(\mathbf{k}, \mathbf{q})$ on the fine grid to obtain a complete $g_{m\nu}(\mathbf{k}, \mathbf{q})$. Using the long-range scattering potential $V_{\mathbf{q}\kappa\alpha}^{\mathcal{L}}$ which refers to the displacement of atom κ in the direction α along a phonon mode \mathbf{q} , the expression of $g_{m\nu}^{\mathcal{L}}(\mathbf{k}, \mathbf{q})$ is given as [21, 38]

$$g_{mn\nu}^{\mathcal{L}}(\mathbf{k}, \mathbf{q}) = \left[\frac{\hbar}{2\omega_\nu(\mathbf{q})} \right]^{\frac{1}{2}} \sum_{\kappa\alpha} \frac{e_{\kappa\alpha\nu}(\mathbf{q})}{\sqrt{M_\kappa}} \sum_{sp} \times U_{m\mathbf{s}\mathbf{k}+\mathbf{q}} \langle u_{\mathbf{s}\mathbf{k}+\mathbf{q}}^{\mathbf{W}} | V_{\mathbf{q}\kappa\alpha}^{\mathcal{L}} | u_{\mathbf{p}\mathbf{k}}^{\mathbf{W}} \rangle U_{\mathbf{p}\mathbf{k}}^\dagger, \quad (5)$$

where $e_{\kappa\alpha\nu}$ is the phonon eigenvector, M_κ is the atomic mass, $U_{m\mathbf{s}\mathbf{k}}$ denotes the Wannier rotation matrices applied to the periodic part of the wavefunctions expressed in the Wannier basis $|u_{n\mathbf{k}}^{\mathbf{W}}\rangle$.

Truncating the expansion at the order of $\mathcal{O}(\mathbf{q})$, the long-range scattering potential is given as [12]

$$V_{\mathbf{q}\kappa\alpha}^{\mathcal{L}}(\mathbf{r}) = \frac{\pi e}{S_{\text{uc}}} \frac{f(|\mathbf{q}|)}{|\mathbf{q}|} e^{-i\mathbf{q}\cdot\boldsymbol{\tau}_\kappa} \left[\frac{1}{\tilde{\epsilon}^{\parallel}(\mathbf{q})} \left\{ 2i\mathbf{q} \cdot \mathbf{Z}_{\kappa\alpha} + \mathbf{q} \cdot \mathbf{q} \cdot \mathbf{Q}_{\kappa\alpha} - |\mathbf{q}|^2 Q_{\kappa\alpha z z} - 2\mathbf{q} \cdot \mathbf{Z}_{\kappa\alpha} \mathbf{q} \cdot V^{\text{Hxc}, \mathcal{E}}(\mathbf{r})/e \right\} + \frac{1}{\tilde{\epsilon}^{\perp}(\mathbf{q})} \left\{ 2|\mathbf{q}|^2 Z_{\kappa\alpha z} [z + V^{\text{Hxc}, \mathcal{E}_z}(\mathbf{r})/e] \right\} \right], \quad (6)$$

where $V^{\text{Hxc}, \mathcal{E}}$ denotes the self-consistent potential change induced by the electric field perturbation, $\boldsymbol{\tau}_\kappa$ denotes the position of atom κ within the cell, $\mathbf{Z}_{\kappa\alpha}$ is the dynamical dipole along α direction, and $\mathbf{Q}_{\kappa\alpha}$ is the dynamical quadrupole. The range separation function $f(|\mathbf{q}|) = 1 - \tanh(|\mathbf{q}|L/2)$ is a low-pass Fourier filter that ensures the macroscopic character of the potential, where the parameter L defines the length scale. $\tilde{\epsilon}^{\parallel}$ and $\tilde{\epsilon}^{\perp}$ are the dielectric functions given by Eqs. (38)-(39) in Ref. [12]. The above parameters of III-V monolayers are given in Table II.

Beside the expansion of $V_{\mathbf{q}\kappa\alpha}^{\mathcal{L}}$, the Wannier-gauge eigenstates are also expanded to the first order of Taylor series as

$$\langle u_{\mathbf{s}\mathbf{k}+\mathbf{q}}^{\mathbf{W}} | = \langle u_{\mathbf{s}\mathbf{k}}^{\mathbf{W}} | + \sum_{\alpha} q_{\alpha} \left\langle \frac{\partial u_{\mathbf{s}\mathbf{k}}^{\mathbf{W}}}{\partial k_{\alpha}} \right|. \quad (7)$$

By introducing the Berry connection $A_{sp\mathbf{k},\alpha}^{\mathbf{W}} \equiv -i \langle \frac{\partial u_{\mathbf{s}\mathbf{k}}^{\mathbf{W}}}{\partial k_{\alpha}} | u_{\mathbf{p}\mathbf{k}}^{\mathbf{W}} \rangle$ and $\varphi_{\mathbf{q}}$ as the form factor for $V_{\mathbf{q}\kappa\alpha}^{\mathcal{L}}$, we obtain

$$\langle u_{\mathbf{s}\mathbf{k}+\mathbf{q}}^{\mathbf{W}} | \varphi_{\mathbf{q}} | u_{\mathbf{p}\mathbf{k}}^{\mathbf{W}} \rangle \approx \delta_{sp} + i\mathbf{q} \cdot \left[\langle u_{\mathbf{s}\mathbf{k}}^{\mathbf{W}} | V^{\mathcal{E}} | u_{\mathbf{p}\mathbf{k}}^{\mathbf{W}} \rangle + \mathbf{A}_{sp\mathbf{k}}^{\mathbf{W}} \right]. \quad (8)$$

The term of $V^{\mathcal{E}}$ in Eq. (8) is omitted in our calculations due to its negligible contribution [18, 21]. The term of $\mathbf{A}_{sp\mathbf{k}}^{\mathbf{W}}$ involves the Berry connection, which is crucial since it ensures the smoothness of $g_{mn\nu}^{\mathcal{L}}(\mathbf{k}, \mathbf{q})$ and restores gauge covariance to the lowest order in \mathbf{q} [12, 21].

The effects of two corrections mentioned above, namely the dynamical quadrupole and the Berry connection, on the carrier mobility in III-V 2D semiconductors are investigated in the present section. The standard pseudopotential and SOC are applied to the calculations. The quality of the Wannier interpolations are checked with the deformation potentials of the InAs monolayer. Figure 4 shows the result of the Wannier interpolation without Berry connection, which leads to slight deviations from DFPT results for the LO modes. Figure 5 presents the

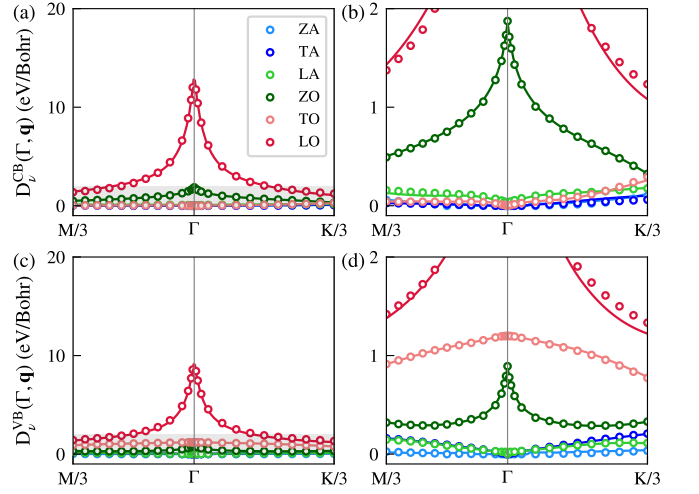


FIG. 4. Comparison between the InAs deformation potentials of DFPT and Wannier interpolation. Dynamical quadrupoles are considered while the Berry connection is neglected for the Wannier interpolation. Conduction (a) and valence (c) bands are given in the left column, the corresponding zoomed-in figures (b) and (d) of the shadowed region from 0 to 2 eV/Bohr are given in the right column.

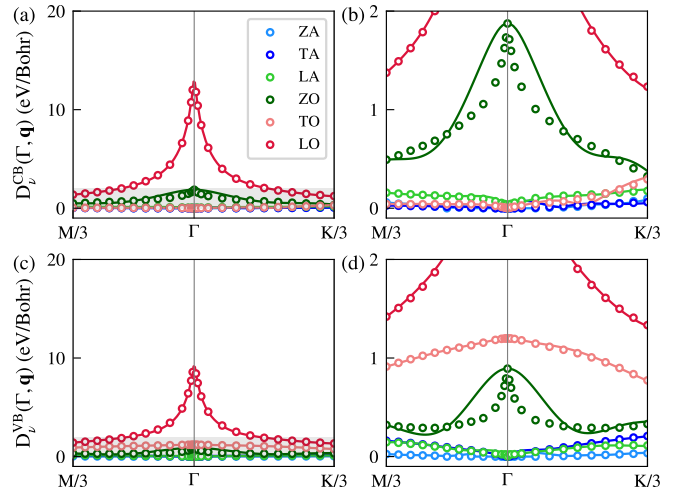


FIG. 5. Comparison between the InAs deformation potentials of DFPT and Wannier interpolation in the absence of both dynamical quadrupole and Berry connection. Conduction (a) and valence (c) bands are given in the left column, the corresponding zoomed-in figures (b) and (d) of the shadowed region from 0 to 2 eV/Bohr are given in the right column.

Wannier result in the absence of both Berry connection and dynamical quadrupole. For the ZO mode, neglecting quadrupole introduces large deviations from the DFPT results for both conduction and valence bands.

Figure 6 shows the impacts on the mobilities caused by the two types of corrections. For μ^e in phosphides, the impact of Berry connection is large since the ZA, ZO, and TO modes are not well interpolated, see details in Fig. S4 and Fig. S6 in SM [35]. In other cases, the impact of the Berry connection is limited to 10%, attributed to the relatively good fittings as manifested by the InAs result in Fig. 4. Further neglecting

dynamical quadrupole leads to a mobility underestimation for both electron and hole for all the III-V monolayers. The underestimation can reach up to 40% for the electron mobilities of all the materials, as well as for the hole mobilities in InAs and antimonides. Regarding phosphides and GaAs where the hole mobilities are strongly suppressed by band structures with multi-peaks in BZ, the effect of quadrupole is also suppressed. Note that this conclusion, i.e. neglecting quadrupole will underestimate the mobility, can not be generalized for all the materials, since scattering rates depend on not only the EPC matrix elements but also on the conservation of energies and momenta. Moreover, Fig. 5 shows that the behavior of Wannier deformation potential of ZO mode is not systematic, namely, Wannier deformation potential is higher than the DFPT around Γ but lower away from Γ . Thus, the influence of neglecting quadrupole can only be given by calculations. In any case, neglecting quadrupole will lower the quality of the Wannier interpolation, leading to unconvincing computational results.

The behavior of the carrier mobility can be interpreted by the scattering rates, which can be decomposed by phonon energy. Here, we focus on the electron mobility in InAs monolayer. Considering the energy of $3/2k_B T = 39$ meV away from the band edge (see details in Ref. [39]), the phonon energy resolved scattering rates τ^{-1} , computed in the presence or in the absence of both corrections, are respectively presented in Figs. 7(a) and (b). The total scattering rate is enhanced by the absence of corrections from 48 to 68 THz, increased by $\sim 40\%$, demonstrating the main influence is caused by the dynamical quadrupole. In both cases, the scatterings are determined by the high-frequency phonons, i.e., the LO mode. Indeed, InAs is a polar material with one isotropic and parabolic conduction band, and its behavior can be described by the Fröhlich model [40]. Since quadrupole has negligible influence on the LO mode, the scatterings contributed by the LO mode (the area of the right peak) is nearly unchanged. On the other

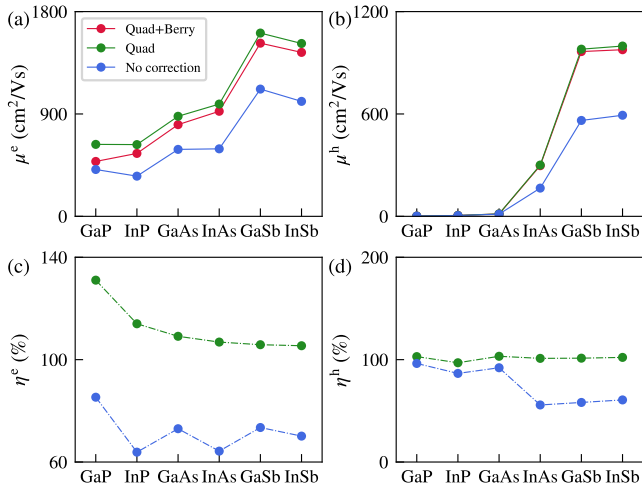


FIG. 6. Electron (a) and hole (b) mobilities calculated with and without corrections according to #2, #4, and #5 methodologies. Taking the result with quadrupole and Berry connection as a benchmark, variations of the results of neglecting Berry connection and neglecting both corrections are given as ratios in (c) for electron and (d) for hole, respectively.

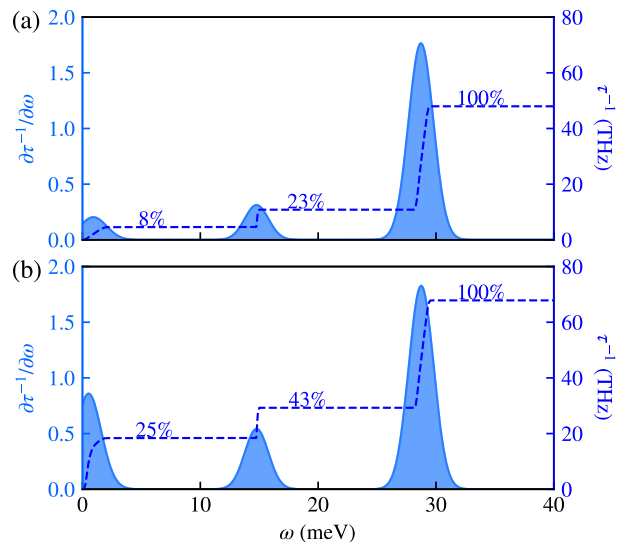


FIG. 7. Spectral decomposition of the electron scattering rates as a function of phonon energy of InAs monolayer (a) in the presence and (b) in the absence of both dynamical quadrupole and Berry connection. The peaks represent $\partial\tau^{-1}/\partial\omega$ (left axis), and the dashed lines represent the cumulative integral τ^{-1} (right axis). The percentages indicate the cumulative contribution to the total value of τ^{-1} .

hand, the quadrupole strongly affects the ZO mode. When the quadrupole is neglected, the scattering contributed by the ZO mode is enhanced from 7.2 to 12.2 THz given by the areas of middle peaks, explaining the mobility underestimation by the absence of quadrupole. The above discussion illustrates that the impacts of Berry connection are materials dependent. More importantly, the dynamical quadrupole can strongly affect the computed mobility by up to 40% for materials with high mobilities, illustrating the necessity to include quadrupole for their accurate predictions.

IV.3. Impact of spin-orbit coupling

Arising from the interaction between the spin and orbital angular momenta, SOC impacts the motion of electrons and modifies the electronic structures, especially for materials with heavy atoms. In the fully-relativistic calculation including SOC [see Fig. 1(b)], the conduction band minimum (CBM) presents a Rashba splitting at the Γ point, analog to a single valley in the BZ. In InAs monolayer, the VBM is also located at the Γ point where the SOC splitting occurs, and $\varepsilon_K = E_F - 88$ meV. In the scalar-relativistic case [see Fig. 8], the edge of the conduction band becomes a single valley at the Γ point, and the valence bands are changed: the VBM is moved to the K point, the degeneracy at the Γ point is recovered due to crystal symmetry, and $\varepsilon_\Gamma = E_F - 19$ meV. The modifications are even more striking in GaSb and InSb, see Fig. S11 and Fig. S13 in SM [35]. In contrast to the electronic structure, SOC induces a negligible change to the phonon dispersion as shown in Fig. S9 in SM [35], since the phonon dispersion is associated with lattice vibrations which are primarily determined by the masses of the nuclei and the interatomic forces in the lattice. The deformation potential

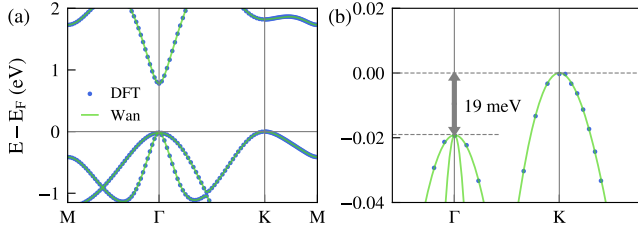


FIG. 8. InAs monolayer electronic band structure (a) calculated without SOC, and the corresponding zoomed-in figure (b) around Fermi energy.

from the SR calculation is very similar to that from the FR calculation, see Fig. S10 in SM [35].

The comparisons between the FR and SR calculated mobilities are shown in Fig. 9. The absence of SOC causes limited changes in electron mobilities for all materials, while more prominent variations emerge in hole mobilities. For phosphides and GaAs, the hole mobilities are strongly suppressed in both cases, since the VBMs are always located at the K points in these materials. For InAs and antimonides, the hole mobilities are greatly suppressed by the absence of SOC.

The significant influence caused by SOC can be explained by the scattering rates of holes. The k -resolved scattering rates in FR and SR calculations of InAs monolayer are respectively presented in Figs. 10(a) and (b). Compared with the FR scattering rates, SR scattering rates are enhanced especially around the K points. This is because in the FR calculation, the VBM is located at the Γ point which is a single scattering peak. Besides, eigenstates at the Γ and K points are separated by a large energy of 88 meV, increasing the barrier of scattering between Γ and K. In contrast, in the SR case, the VBMs are located at the K points which present multi-peaks of scattering in the BZ. Moreover, the energy barrier between eigenstates at the Γ and K points is reduced to 19 meV, increasing the interpeak scatter-

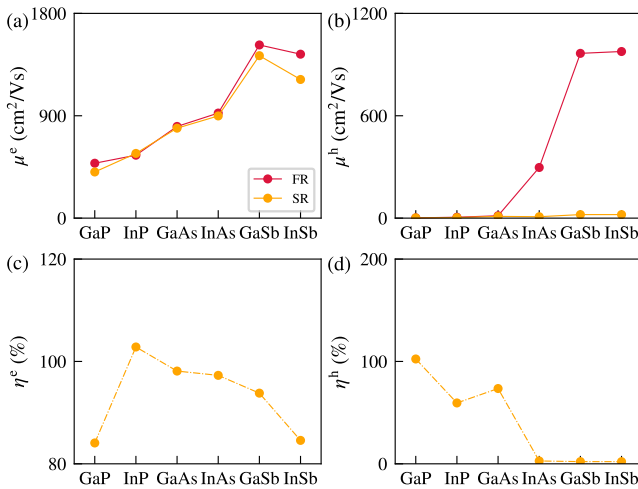


FIG. 9. Electron (a) and hole (b) mobilities calculated with FR and SR according to #2 and #6 methodologies. Taking the FR result as a benchmark, variations of the SR result are given as ratios in (c) for electron and (d) for hole, respectively.

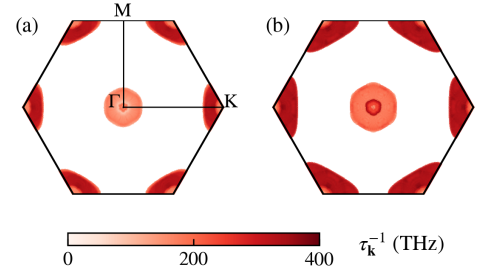


FIG. 10. Momentum-resolved scattering rates of holes in InAs monolayer in (a) FR and (b) SR calculations, given by $\tau_{\mathbf{k}}^{-1} = \frac{1}{N^w} \sum_n \tau_{n\mathbf{k}}^{-1}$.

ing. Consequently, the hole mobility in the SR calculation is notably reduced.

Additional understanding of the hole mobility can be gained by mode-resolved scattering analysis, whose behavior is determined by the electron and phonon dispersions due to the energy and momentum conservations. Figure 11(a) shows that in the FR calculation, the LO mode makes the dominant contribution in the energy range from VBM to $\varepsilon_K = -88$ meV, since there is only one band peak at the Γ point, analog to a Fröhlich system. The increase at -30 meV is attributed to the LO mode with $\omega_{LO} \approx 30$ meV. Below ε_K , multi-peaks at K points are involved in the Fermi surface window, and the ZA mode starts to contribute to the intrapeak and interpeak scatterings with small phonon energies. As indicated by Fig. 11(b), in the FR case, ZA phonons dominate the scattering due to the intrapeak scattering at K point. A sharp increase of ZA contribution occurs around -4 meV since more phonons of $\omega_{ZA} \approx 4$ meV at $\mathbf{q} = \mathbf{K}$ point [see Fig. 1(e)] are enabled for interpeak scatterings between K points in k -space. When $\varepsilon_{\Gamma} = -19$ meV enters into the Fermi surface window, ZA contribution is further enhanced by the interpeak scattering between the Γ and K points. Furthermore, expanding the Fermi surface window allows LO mode with $\omega_{LO} \approx 30$ meV to participate in the scattering. Since more phonons are involved, the scattering is

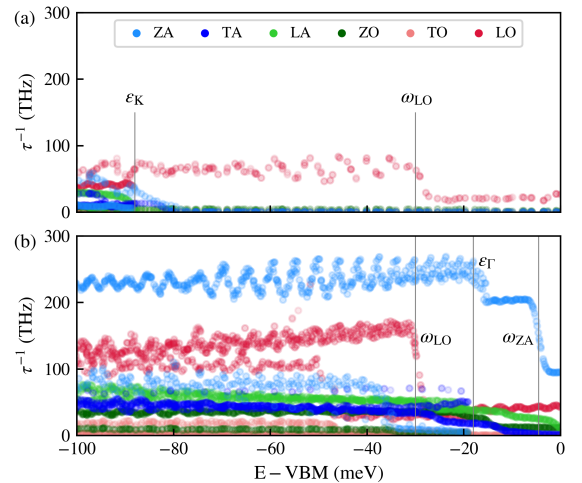


FIG. 11. Mode-resolved scattering rates of hole mobility in InAs monolayer in (a) FR and (b) SR calculations.

enhanced in the SR calculation. The above discussion shows that SOC can significantly modify the electronic structure and lead to large mobility variations $\sim 100\%$, demonstrating the importance of considering SOC, especially for materials with heavy atoms and multi-band edges.

IV.4. Balance between accuracy and cost

Although SOC induces significant changes in the electronic structures, it negligibly affects the phonon dispersion and scattering potential variation. Considering the cost of DFPT calculations, we can use the electronic wavefunctions from the FR calculation and the scattering potential variations from the SR calculation to perform the Wannier interpolation for EPC computation. The quality of the interpolation has been validated by the corresponding Wannier and DFPT deformation potentials as shown in Fig. S10 in SM [35].

Figure 12 presents the comparison between the complete FR calculation and the mix methodology. For the electron mobility, the discrepancies are limited below 3%, while for the hole mobility, the discrepancies can be up to 7% in GaP and InSb. Still, the mix methodology produces a result consistent with the complete FR calculation, demonstrating its effectiveness.

Although paying a small accuracy loss, the mix methodology can significantly enhance the calculation efficiency. The computational costs of various methodologies mentioned above are summarized in Fig. 13 where dynamical quadrupole and Berry connection are always considered. DFPT is always the most expensive calculation for all methodologies. The valencePP+FR and standardPP+SR methodologies are inexpensive but unreliable. Both standardPP+FR and stringentPP+FR produce consistent results, while the latter is more expensive since more semi-core states are included. The standardPP+mix methodology exhibits the same computational cost as the standardPP+SR in DFPT calculation, and the similar computational cost to the

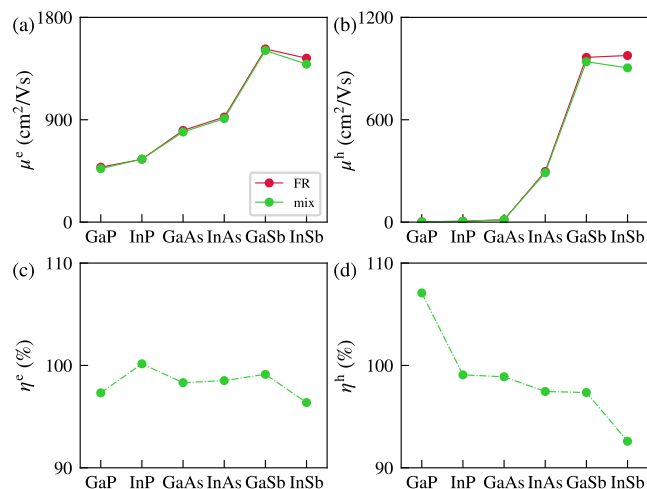


FIG. 12. Electron (a) and hole (b) mobilities calculated with the FR and the mix scheme according to #2 and #7 methodologies. Taking the FR result as a benchmark, variations of the mix methodology are given as ratios in (c) for electron and (d) for hole, respectively.

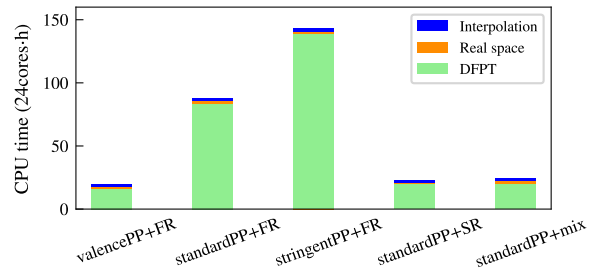


FIG. 13. Computational costs for different methodologies in InAs monolayer. DFPT denotes the phonon calculation for potential variation with a self-consistency threshold of 10^{-18} . Real space denotes the EPW calculation for representation transform from reciprocal to real space on the coarse grid. Interpolation denotes the interpolation from real to reciprocal space for transport properties on fine grid. All the calculations are performed using 24 AMD EPYC 7H12 cores with a base clock speed of 2.6 GHz.

standardPP+FR in EPW calculation. Consequently, the total cost of standardPP+mix methodology significantly decreases, which is 28% of the standardPP+FR cost, and 17% of the stringentPP+FR cost. The above discussion suggests that the standardPP+mix methodology can strike a good balance between accuracy and cost.

V. TEMPERATURE-DEPENDENT MOBILITIES

To show the most accurate results, we present the temperature-dependent mobilities calculated by the standardPP+Quad+Berry+FR methodology in Fig. 14. All the mobilities go down with increasing temperature. For the electron mobilities, all materials present a high μ^e over $100 \text{ cm}^2/\text{Vs}$, attributed to the single valley of conduction bands. The mobilities increase with the atomic number due to the decreasing effective mass, and the antimonides can reach $\mu^e \approx 10^4 \text{ cm}^2/\text{Vs}$ at 100 K. The decay of μ^e can be one order of magnitude from 100 K to 500 K. For the hole mobilities, μ^h decays much faster with temperature. Still, antimonides can present high hole mobilities thanks to their single-peak VBMs.

Instead of drift mobility, Hall mobility is more commonly measured experimentally, since it can be determined using a well-established setup, i.e., the Hall effect measurement. Indeed, such a transport measurement is performed under an external magnetic field, which induces a Lorentz force on the carriers and then changes the drift mobility μ to be the Hall mobility μ^H . Denoting the ratio between the Hall mobility and the drift mobility, the Hall factor is commonly assumed to be unity [41]. However, the suitability of this assumption should be carefully evaluated. The Hall mobility can be calculated by adding the external magnetic field to the BTE, see details in Eqs. (6)-(9) in Ref. [27]. In the present computations of Hall factors, we apply an external magnetic field along z direction with $B_z = 10^{-10} \text{ T}$, and we focus on the tensor element r_{xy}^H which indicates the ratio of μ_{xy}^H over μ_{xx} , the subscripts will be omitted in the following discussions.

Figure 15 presents the temperature-dependent Hall mobilities

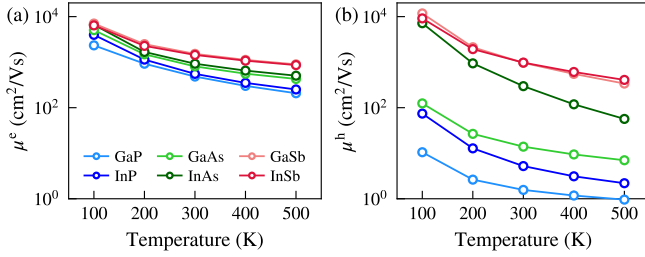


FIG. 14. Temperature-dependent (a) electron and (b) hole drift mobilities.

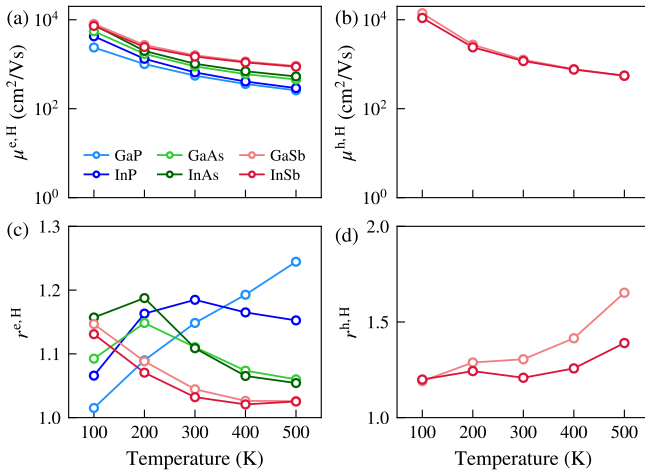


FIG. 15. Temperature-dependent (a) electron and (b) hole Hall mobilities, as well as (c) electron and (d) hole Hall factors.

and Hall factors, depicting the materials with high mobilities which are more promising for experiments. For the electron transport, the magnetic field introduces limited changes to the mobility, as demonstrated by $r^{e,H}$ which is below 1.3 in all the materials. However, for the hole transport, $r^{h,H}$ can be as large as 1.7, as shown by the GaSb monolayer at high temperature. These theoretical results demonstrate that the unitary Hall factor can be a rough approximation, which may sometimes lead to the overestimation of the drift mobility in experiments.

VI. SUMMARY

Carrier mobilities investigated using DFPT and Wannier functions are reported herewith for 6 semiconductors in the III-V monolayer family. The quality of the Wannier interpolation has been validated by the comparison with DFPT calculations. To show the impacts induced by different approximations, several methodologies have been proposed to investigate the influences on mobilities caused by semi-core states, dynamical quadrupole, Berry connection, and spin-orbit coupling. Semi-core states in pseudopotentials are found to be essential for accurate mobility calculations, dynamical quadrupole can induce a variation of $\sim 40\%$, Berry connection causes an impact of $\sim 10\%$, and SOC can even yield an influence of $\sim 100\%$ for materials with multi-peak electronic structures. The different mechanisms are interpreted by the momentum- and mode-resolved scattering rates. Besides, DFPT results are negligibly affected by SOC, which can be neglected to accelerate computation with a precision loss of less than 7%. After evaluating the various methodologies, temperature-dependent drift mobilities are computed, illustrating that the temperature can change the mobilities by one or two orders of magnitude, and the Hall factors range from 1.0 to 1.7. From the point of view of *ab initio* modeling, it is mandatory and commonly accepted to implement certain approximations. Consequently, it is crucial to understand the extent of their impacts and evaluate their suitability. Striking the balance between accuracy and cost, this research can definitely provide guidelines for accurate and efficient calculations of carrier mobilities in 2D semiconductors.

ACKNOWLEDGMENTS

The authors would like to thank Matteo Giantomassi for fruitful discussions. S. P. acknowledges the support from the Fonds de la Recherche Scientifique de Belgique (F.R.S.-FNRS). J. Z. and J.-C.C. acknowledge financial support from the Fédération Wallonie-Bruxelles through the ARC Grant “DREAMS” (No. 21/26-116), from the EOS project “CONNECT” (No. 40007563), and from the Belgium F.R.S.-FNRS through the research project (No. T.029.22F). Computational resources have been provided by the PRACE award granting access to MareNostrum4 at Barcelona Supercomputing Center (BSC), Spain and Discoverer in SofiaTech, Bulgaria (OptoSpin project ID. 2020225411), and by the Consortium des Équipements de Calcul Intensif (CÉCI), funded by the F.R.S.-FNRS under Grant No. 2.5020.11 and by the Walloon Region, as well as computational resources awarded on the Belgian share of the EuroHPC LUMI supercomputer.

[1] C. Zhang and Y. Liu, Phonon-limited transport of two-dimensional semiconductors: Quadrupole scattering and free carrier screening, *Phys. Rev. B* **106**, 115423 (2022).
 [2] X. Liu and M. C. Hersam, 2D materials for quantum information science, *Nat. Rev. Mater.* **4**, 669 (2019).

[3] J. Zhou, S. Poncé, and J.-C. Charlier, Enhanced Spin Hall Ratio in Two-Dimensional Semiconductors (accompanying manuscript) (2024).
 [4] F. Wu, H. Tian, Y. Shen, Z. Hou, J. Ren, G. Gou, Y. Sun, Y. Yang, and T.-L. Ren, Vertical MoS₂ transistors with sub-1-nm gate lengths, *Nature* **603**, 259 (2022).

- [5] Y. Shen, Z. Dong, Y. Sun, H. Guo, F. Wu, X. Li, J. Tang, J. Liu, X. Wu, H. Tian, and T.-L. Ren, The Trend of 2D Transistors toward Integrated Circuits: Scaling Down and New Mechanisms, *Adv. Mater.* **34**, 2201916 (2022).
- [6] F. Giustino, Electron-phonon interactions from first principles, *Rev. Mod. Phys.* **89**, 015003 (2017).
- [7] F. Giustino, M. L. Cohen, and S. G. Louie, Electron-phonon interaction using Wannier functions, *Phys. Rev. B* **76**, 165108 (2007).
- [8] C.-H. Park, N. Bonini, T. Sohier, G. Samsonidze, B. Kozinsky, M. Calandra, F. Mauri, and N. Marzari, Electron-Phonon Interactions and the Intrinsic Electrical Resistivity of Graphene, *Nano Lett.* **14**, 1113 (2014).
- [9] L. Cheng, C. Zhang, and Y. Liu, The Optimal Electronic Structure for High-Mobility 2D Semiconductors: Exceptionally High Hole Mobility in 2D Antimony, *J. Am. Chem. Soc.* **141**, 16296 (2019).
- [10] T. Sohier, D. Campi, N. Marzari, and M. Gibertini, Mobility of two-dimensional materials from first principles in an accurate and automated framework, *Phys. Rev. Mater.* **2**, 114010 (2018).
- [11] T. Sohier, M. Gibertini, D. Campi, G. Pizzi, and N. Marzari, Valley-Engineering Mobilities in Two-Dimensional Materials, *Nano Lett.* **19**, 3723 (2019).
- [12] S. Poncé, M. Royo, M. Stengel, N. Marzari, and M. Gibertini, Long-range electrostatic contribution to electron-phonon couplings and mobilities of two-dimensional and bulk materials, *Phys. Rev. B* **107**, 155424 (2023).
- [13] W.-H. Xiao, B. Zeng, Z.-K. Ding, H. Pan, W.-W. Liu, Q.-Q. Li, K. Yang, N. Luo, J. Zeng, K.-Q. Chen, and L.-M. Tang, Exceptionally high hole mobilities in monolayer group-IV monochalcogenides GeTe and SnTe, *Appl. Phys. Lett.* **123**, 10.1063/5.0142613 (2023).
- [14] C. Zhang, R. Wang, H. Mishra, and Y. Liu, Two-Dimensional Semiconductors with High Intrinsic Carrier Mobility at Room Temperature, *Phys. Rev. Lett.* **130**, 087001 (2023).
- [15] S. Song, Y. Sun, S. Liu, J.-H. Yang, and X.-G. Gong, General rules and applications for screening high phonon-limited mobility in two-dimensional semiconductors, *Phys. Rev. B* **107**, 155101 (2023).
- [16] N. Hasani, A. Rajabi-Maram, and S. B. Touski, Effects of spin-orbit coupling on the electronic properties of the buckled III-V monolayers, *J. Magn. Magn. Mater.* **543**, 168638 (2022).
- [17] M. J. van Setten, M. Giantomassi, E. Bousquet, M. J. Verstraete, D. R. Hamann, X. Gonze, and G.-M. Rignanese, The PseudoDojo: Training and grading a 85 element optimized norm-conserving pseudopotential table, *Comput. Phys. Commun.* **226**, 39 (2018).
- [18] G. Brunin, H. P. C. Miranda, M. Giantomassi, M. Royo, M. Stengel, M. J. Verstraete, X. Gonze, G.-M. Rignanese, and G. Hautier, Electron-Phonon beyond Fröhlich: Dynamical Quadrupoles in Polar and Covalent Solids, *Phys. Rev. Lett.* **125**, 136601 (2020).
- [19] G. Brunin, H. P. C. Miranda, M. Giantomassi, M. Royo, M. Stengel, M. J. Verstraete, X. Gonze, G.-M. Rignanese, and G. Hautier, Phonon-limited electron mobility in Si, GaAs, and GaP with exact treatment of dynamical quadrupoles, *Phys. Rev. B* **102**, 094308 (2020).
- [20] V. A. Jhalani, J.-J. Zhou, J. Park, C. E. Dreyer, and M. Bernardi, Piezoelectric Electron-Phonon Interaction from Ab Initio Dynamical Quadrupoles: Impact on Charge Transport in Wurtzite GaN, *Phys. Rev. Lett.* **125**, 136602 (2020).
- [21] S. Poncé, M. Royo, M. Gibertini, N. Marzari, and M. Stengel, Accurate Prediction of Hall Mobilities in Two-Dimensional Materials through Gauge-Covariant Quadrupolar Contributions, *Phys. Rev. Lett.* **130**, 166301 (2023).
- [22] S. Poncé, W. Li, S. Reichardt, and F. Giustino, First-principles calculations of charge carrier mobility and conductivity in bulk semiconductors and two-dimensional materials, *Rep. Prog. Phys.* **83**, 036501 (2020).
- [23] S. Poncé, E. R. Margine, and F. Giustino, Towards predictive many-body calculations of phonon-limited carrier mobilities in semiconductors, *Phys. Rev. B* **97**, 121201(R) (2018).
- [24] P. Giannozzi, O. Andreussi, T. Brumme, O. Bunau, M. B. Nardelli, M. Calandra, R. Car, C. Cavazzoni, D. Ceresoli, M. Cococcioni, N. Colonna, I. Carnimeo, A. Dal Corso, S. de Gironcoli, P. Delugas, R. A. DiStasio, A. Ferretti, A. Floris, G. Fratesi, G. Fugallo, R. Gebauer, U. Gerstmann, F. Giustino, T. Gorni, J. Jia, M. Kawamura, H.-Y. Ko, A. Kokalj, E. Küçükbenli, M. Lazzeri, M. Marsili, N. Marzari, F. Mauri, N. L. Nguyen, H.-V. Nguyen, A. Otero-de-la Roza, L. Paulatto, S. Poncé, D. Rocca, R. Sabatini, B. Santra, M. Schlipf, A. P. Seitsonen, A. Smogunov, I. Timrov, T. Thonhauser, P. Umari, N. Vast, X. Wu, and S. Baroni, Advanced capabilities for materials modelling with Quantum ESPRESSO, *J. Phys.: Condens. Matter* **29**, 465901 (2017).
- [25] T. Sohier, M. Calandra, and F. Mauri, Density functional perturbation theory for gated two-dimensional heterostructures: Theoretical developments and application to flexural phonons in graphene, *Phys. Rev. B* **96**, 075448 (2017).
- [26] S. Poncé, E. Margine, C. Verdi, and F. Giustino, Epw: Electron-phonon coupling, transport and superconducting properties using maximally localized wannier functions, *Computer Physics Communications* **209**, 116 (2016).
- [27] H. Lee, S. Poncé, K. Bushick, S. Hajinazar, J. Lafuente-Bartolome, J. Leveillee, C. Lian, J.-M. Lihm, F. Macheda, H. Mori, H. Paudyal, W. H. Sio, S. Tiwari, M. Zacharias, X. Zhang, N. Bonini, E. Kioupakis, E. R. Margine, and F. Giustino, Electron-phonon physics from first principles using the EPW code, *npj Comput. Mater.* **9**, 1 (2023).
- [28] X. Gonze, B. Amadon, G. Antonius, F. Arnardi, L. Baguet, J.-M. Beuken, J. Bieder, F. Bottin, J. Bouchet, E. Bousquet, N. Brouwer, F. Bruneval, G. Brunin, T. Cavignac, J.-B. Charraud, W. Chen, M. Côté, S. Cottenier, J. Denier, G. Geneste, P. Ghosez, M. Giantomassi, Y. Gillet, O. Gingras, D. R. Hamann, G. Hautier, X. He, N. Helbig, N. Holzwarth, Y. Jia, F. Jollet, W. Lafargue-Dit-Hauret, K. Lejaeghere, M. A. L. Marques, A. Martin, C. Martins, H. P. C. Miranda, F. Naccarato, K. Persson, G. Petretto, V. Planes, Y. Pouillon, S. Prokhorenko, F. Ricci, G.-M. Rignanese, A. H. Romero, M. M. Schmitt, M. Torrent, M. J. van Setten, B. Van Troeye, M. J. Verstraete, G. Zerah, and J. W. Zwanziger, The ABINIT project: Impact, environment and recent developments, *Comput. Phys. Commun.* **248**, 107042 (2020).
- [29] M. Royo and M. Stengel, First-Principles Theory of Spatial Dispersion: Dynamical Quadrupoles and Flexoelectricity, *Phys. Rev. X* **9**, 021050 (2019).
- [30] <https://github.com/PseudoDojo/ONCVSP-PBE-SR-noCCv0.4>.
- [31] J. Zhou, S. Poncé, and J.-C. Charlier, *Materials Cloud Archive*, See the record in account. Username: jiaqi.zhou@uclouvain.be; Password: Referees.
- [32] K. Wu, J. Chen, H. Ma, L. Wan, W. Hu, and J. Yang, Two-Dimensional Giant Tunable Rashba Semiconductors with Two-Atom-Thick Buckled Honeycomb Structure, *Nano Lett.* **21**, 740 (2021).
- [33] H. L. Zhuang, A. K. Singh, and R. G. Hennig, Computational discovery of single-layer III-V materials, *Phys. Rev. B* **87**, 165415 (2013).
- [34] H. Şahin, S. Cahangirov, M. Topsakal, E. Bekaroglu, E. Akturk, R. T. Senger, and S. Ciraci, Monolayer honeycomb structures of group-IV elements and III-V binary compounds: First-principles

- calculations, *Phys. Rev. B* **80**, 155453 (2009).
- [35] J. Zhou, S. Poncé, and J.-C. Charlier, Supplementary Material (2024).
- [36] S. Poncé, F. Macheda, E. R. Margine, N. Marzari, N. Bonini, and F. Giustino, First-principles predictions of Hall and drift mobilities in semiconductors, *Phys. Rev. Res.* **3**, 043022 (2021).
- [37] P. Vogl, Microscopic theory of electron-phonon interaction in insulators or semiconductors, *Phys. Rev. B* **13**, 694 (1976).
- [38] C. Verdi and F. Giustino, Fröhlich Electron-Phonon Vertex from First Principles, *Phys. Rev. Lett.* **115**, 176401 (2015).
- [39] S. Poncé, M. Schlipf, and F. Giustino, Origin of Low Carrier Mobilities in Halide Perovskites, *ACS Energy Lett.* **4**, 456 (2019).
- [40] F. Herbert, Interaction of electrons with lattice vibrations, *Proc. R. Soc. London A - Math. Phys. Sci.* **215**, 291 (1952).
- [41] D. K. Schroder, *Semiconductor Material and Device Characterization* (Wiley-IEEE Press, 2015).